This is author's post-print before final IEEE editing and formatting. The paper is published as:
C. Liang and E. J. Fielding, "Measuring azimuth deformation with L-band ALOS-2 ScanSAR interferometry," IEEE Transactions on Geoscience and Remote Sensing, vol. 55, no. 5, pp. 2725-2738, May 2017. DOI: 10.1109/TGRS.2017.2653186

Measuring Azimuth Deformation With L-band ALOS-2 ScanSAR Interferometry

Cunren Liang and Eric J. Fielding[1]

Abstract

We analyze the methods for measuring azimuth deformation with L-band ALOS-2 ScanSAR interferometry. To implement the methods, we extract focused bursts from the ALOS-2 full-aperture product, which is the only product available for ScanSAR interferometry at present. The extracted bursts are properly processed to measure azimuth deformation using interferometric phase. We apply the range split-spectrum method to ScanSAR to estimate the differential ionospheric phase of the interferogram, and take the azimuth derivative of the differential ionospheric phase to mitigate the relative azimuth shift caused by ionosphere. For the first time, azimuth deformation of a large earthquake (April 25, 2015 Nepal earthquake) is nearly completely measured by L-band ScanSAR interferometry with moderate precision. The result is validated by azimuth deformation measured by incoherent cross correlation using a pair of high resolution RADARSAT-2 images. In addition to the final azimuth deformation, we show the possibility of processing full-aperture ScanSAR product using a burst-by-burst approach to form regular interferograms. We also show the recent strong large-scale ionospheric effects on L-band ALOS-2 ScanSAR interferograms. Other possible applications of this research include measuring the movement of glaciers.

Index Terms—scanning synthetic aperture radar (ScanSAR), ALOS-2, earthquake, azimuth deformation, ionosphere.

I. Introduction

Cross correlation (including incoherent and coherent cross correlation) and split spectrum are the two main methods used to measure offsets between two synthetic aperture radar (SAR) images, e.g. ground deformation and coregistration offsets [1]-[3]. In azimuth, the split spectrum is usually referred to as multiple aperture InSAR (MAI) for azimuth deformation measurement [3] in the geophysical community, while as spectral diversity [4] mainly for stringent azimuth coregistration in the SAR signal processing community. To follow the existing conventions, we refer to it as MAI in the context of azimuth deformation measurement, and as spectral diversity in the context of azimuth coregistration.

Azimuth deformation is an important component to construct three-dimensional deformation using SAR images. In a recent paper, a future spaceborne SAR concept has been proposed to measure azimuth deformation using MAI [5]. At present, while MAI method mainly uses stripmap mode data to measure azimuth deformation, many spaceborne SAR systems are designed to be able to operate in ScanSAR mode [6], [7] to acquire wide-swath images. In particular, ScanSAR interferometry [8] is one of the goals of the Japan Aerospace Exploration Agency (JAXA) ALOS-2 mission [9], [10]

[1] The authors are with the Jet Propulsion Laboratory, California Institute of Technology, Pasadena, CA 91109 USA.

launched on May 24, 2014. ALOS-2 has been acquiring L-band ScanSAR data with high burst overlap and small baselines since February, 2015. The advantages of implementing MAI with L-band ALOS-2 ScanSAR data include highly coherent signals and large-scale measurement. The resulting azimuth deformation is particularly important for the study of large earthquakes that usually attract wide interests.

Measuring azimuth deformation with L-band ALOS-2 ScanSAR interferometry is not very straightforward. Focused ALOS-2 ScanSAR data is distributed by JAXA as two kinds of products: the full-aperture product and the burst-by-burst product. Currently, only full-aperture product is usable for interferometry. The full-aperture product is focused by a stripmap focusing algorithm after filling burst gaps with zero echoes [11], and individual bursts are no longer available. To measure azimuth deformation, bursts must be retrieved from the full-aperture product. Furthermore, while burst-by-burst approach for ScanSAR interferometry is mature nowadays, specific problems related to this particular case need to be carefully considered. These include the removal of azimuth non-overlap spectra and the coregistration (including range and azimuth) in the presence of ground deformation, strong ionosphere, and inaccurate geometry. While our main purpose of burst-by-burst interferometric processing is azimuth deformation measurement, the resulting burst-by-burst interferometric processing is also useful in that it can provide another way of processing ALOS-2 full-aperture ScanSAR products, because a large number of these products have been, and probably will be, distributed by JAXA. The major advantage of burst-by-burst processing is the significantly reduced data volume.

Low frequency, e.g. L-band, SAR is more sensitive to ionosphere [12]-[14]. For azimuth deformation measurement, the relative azimuth shift caused by ionosphere should be removed. In our experience of processing a large amount of ALOS-2 data over a number of different areas since 2015, we find that most of the interferograms are strongly affected by ionosphere. The range split-spectrum method, making use of the dispersive nature of the ionosphere, has been proposed to estimate the differential ionospheric phase for InSAR [15], [16]. Based on this method, the L-band SAR of the future NASA-ISRO NISAR mission is designed to have an extra range band that can be used to estimate ionosphere [17]. Recently this method was well demonstrated in [18]. We apply this method to ScanSAR to estimate the differential ionospheric phase of the interferogram.

With the ScanSAR bursts available, MAI interferograms can be formed. The differential ionospheric phase estimated can be used to mitigate the relative azimuth shift caused by the ionosphere. The phase of an MAI interferogram is a combination of the phases caused by azimuth deformation of the ground, relative azimuth shift caused by ionosphere, and offset caused by geometric difference. Properly processing the data to finally separate the azimuth deformation phase from the MAI phase is very important.

In the following sections, we theoretically analyze the methods for measuring azimuth deformation with L-band ALOS-2 ScanSAR interferometry. We then implement the methods by properly processing the data. We present the ALOS-2 ScanSAR interferograms processed using a burst-by-burst approach. We show examples of the strong large-scale ionospheric effect appearing in L-band ALOS-2 ScanSAR interferograms. We show the strong large-scale azimuth deformation caused by April 25, 2015 *Mw*7.8 Gorkha earthquake in Nepal.

II. Theoretical Analysis

A. Measuring Azimuth Deformation With ScanSAR Interferometry

It is known that MAI and spectral diversity actually correspond to each other [1], [19]. We describe in some detail here how the two are related to each other. First of all, in the geophysical community, MAI is explained from a physical or geometric point of view. In the SAR signal processing community, spectral diversity is explained from a signal processing point of view. How the two are exactly related to each other is not very clearly explained in the previous literature. Second, we refer to split spectrum as MAI in the context of azimuth deformation measurement to follow the existing conventions, but for ScanSAR data processing, it's more convenient to explain things from a signal processing point of view.

MAI exploits the phase difference of the forward- and backward-look interferograms to measure azimuth deformation [3]. In stripmap mode, for a target on the ground, the forward and backward looks are shown in Fig. 1(a). For an azimuth deformation x of the target, the deformations measured by the interferograms of the two looks along their corresponding line-of-sight (LOS) directions are

$$\begin{cases} \phi_f = -\dfrac{4\pi}{\lambda} x \sin\theta_{g,f} \\ \phi_b = -\dfrac{4\pi}{\lambda} x \sin\theta_{g,b} \end{cases} \tag{1}$$

where λ is the radar wavelength, $\theta_{g,f}$ and $\theta_{g,b}$ are the squint angles *on the ground*, and subscripts f and b indicate forward and backward looks, respectively. The relationship between the squint angle on the ground θ_g and the actual squint angle θ_{sq} is [20]

$$\frac{\sin\theta_{\text{sq}}}{\sin\theta_g} = \frac{v_g}{v_s} \tag{2}$$

where v_s is the actual satellite velocity along the orbit, and v_g is the velocity of the beam footprint on the ground. According to the relationship between Doppler centroid frequency and squint angle [20]

$$f_{\text{DC}} = \frac{2v_s \sin\theta_{\text{sq}}}{\lambda} = \frac{2v_g \sin\theta_g}{\lambda} \tag{3}$$

equation (1) can be expressed as

$$\begin{cases} \phi_f = -\dfrac{2\pi}{v_g} x f_{\text{DC},f} \\ \phi_b = -\dfrac{2\pi}{v_g} x f_{\text{DC},b} \end{cases} \tag{4}$$

By conjugate multiplication of the forward- and backward-look interferograms, we get the MAI interferogram whose phase is

$$\phi_{\text{MAI}} = \phi_f - \phi_b = -\frac{2\pi}{v_g} x \left(f_{\text{DC},f} - f_{\text{DC},b}\right). \tag{5}$$

Then the azimuth deformation can be derived by inverting equation (5)

$$x = -\frac{\phi_{\mathrm{MAI}} v_g}{2\pi\left(f_{\mathrm{DC},f} - f_{\mathrm{DC},b}\right)}. \tag{6}$$

Note the v_g in the numerator, which indicates x is the deformation *on the ground*.

In ScanSAR mode, SAR antenna cyclically points to several subswaths with different look angles. In each cycle, the SAR system collects a group of echoes for each subswath. The group of echoes is called a burst. By repeating this cycle over several subswaths, a wide-swath image can be acquired. For a multiple look ScanSAR system, which is the case for ALOS-2, each point on the ground is imaged by multiple bursts. Each burst represents a look with a distinct squint angle. Suppose that burst N_f and N_b (e.g. burst 1 and burst 3 of the 2-subswath 3-look ScanSAR system shown in Fig. 1(b)), taking the place of forward and backward looks in stripmap mode shown in Fig. 1(a), are used to measure azimuth deformation, the center frequency difference of the two bursts can be given by

$$\Delta f = f_{\mathrm{DC},f} - f_{\mathrm{DC},b} = -\left(N_f - N_b\right) K_a T_C = n K_a T_C \tag{7}$$

where K_a ($K_a > 0$) is the azimuth frequency modulation (FM) rate, T_C is the burst cycle length, and n is the difference of burst numbers. Replacing the frequency difference with equation (7) in equation (6), the azimuth deformation measured by ScanSAR interferometry is

$$x = -\frac{\phi_{\mathrm{MAI}} v_g}{2\pi n K_a T_C} \tag{8}$$

where ϕ_{MAI} is the phase of the MAI interferogram generated from the two burst interferograms.

Fig. 1 (a) and (b) shows the stripmap and ScanSAR MAI geometries for one target. For multiple targets in azimuth, the corresponding azimuth spectra are shown in Fig. 1 (c) and (d). For the backward or forward look in stripmap mode, the spectrum locations of different targets are the same, but the spectra are captured by radar at different time spans; on the contrary, for a burst in ScanSAR mode, the spectrum locations of different targets are different, but the spectra are captured by radar at the same time span. In any case, the frequency difference between two looks or bursts is the same for all targets.

B. Ionospheric Correction

Since 2015, we have processed a large amount of ALOS-2 ScanSAR data over many areas. Most of the interferograms are strongly affected by ionosphere. The original azimuth deformation measurement also contains the relative azimuth shift caused by ionosphere. Doing ionospheric correction is very important to get usable azimuth deformation measurements.

The two-way phase delay of a SAR signal travelling through the ionosphere can be given by [12], [13], [21]

$$\phi_{\mathrm{ion}} = -\frac{4\pi K}{cf}\int n_e \mathrm{d}h \approx -\frac{4\pi K}{cf}\cdot\frac{1}{\cos(\varphi)}\cdot \mathrm{TEC} \tag{9}$$

where K=40.28 $\mathrm{m^3/s^2}$, c is the vacuum speed of light, f is the range radar frequency, φ is the look angle, TEC is the vertical total electron content, and $\int n_e \mathrm{d}h$ is the total electron content along radar signal travelling path. The phase delay is inversely proportional to radar frequency, and therefore lower frequency signal, such as L-band

signal, is more sensitive to ionosphere. For InSAR, the difference of the TEC when acquiring the master and slave signal causes an additional phase in the interferogram

$$\phi_{\text{ion},d} = \phi_{\text{ion},m} - \phi_{\text{ion},s} = -\frac{4\pi K}{cf} \cdot \frac{1}{\cos(\varphi)} \cdot \Delta\text{TEC} \tag{10}$$

where ΔTEC is the differential TEC.

Unlike troposphere that is much lower, the ionosphere is much higher (~400 km) [12]. Therefore for a target on the ground, the spaceborne radar signal is more likely subjected to the ionospheric change within the azimuth synthetic aperture. According to equation (9), the linear component of the ionospheric change imposes an additional linear phase to the radar signal, and consequently moves the whole Doppler spectrum of the target. Supposing that the azimuth SAR signal is linear FM signal, the azimuth time corresponding to the Doppler spectrum shift is

$$\eta_{\text{ion}} = \frac{1}{K_a} \cdot \frac{1}{2\pi} \cdot \frac{\partial \phi_{\text{ion}}}{\partial \eta} \ [s] \tag{11}$$

where η is the azimuth time. After focusing, the target is thus shifted from its original *ground* azimuth location by

$$x_{\text{ion}} = \frac{1}{2} v_g \eta_{\text{ion}} = \frac{v_g}{K_a} \cdot \frac{1}{4\pi} \cdot \frac{\partial \phi_{\text{ion}}}{\partial \eta} \ [m] \tag{12}$$

Note *the factor 1/2*, which corresponds to the two-way SAR signal. The relative azimuth shift of an InSAR image pair is thus

$$x_{\text{ion},d} = \frac{v_g}{K_a} \cdot \frac{1}{4\pi} \cdot \left(\frac{\partial \phi_{\text{ion,m}}}{\partial \eta} - \frac{\partial \phi_{\text{ion,s}}}{\partial \eta} \right) = \frac{v_g}{K_a} \cdot \frac{1}{4\pi} \cdot \frac{\partial \phi_{\text{ion},d}}{\partial \eta} \ [m] \tag{13}$$

Both this relative azimuth shift and the azimuth deformation contribute to the deformation measured by MAI. If the differential ionospheric phase $\phi_{\text{ion},d}$ is known, the relative azimuth shift can be mitigated to get a more accurate azimuth deformation measurement. Conversely, the relative azimuth shift, derived by either cross correlation [22], [23] or split spectrum (MAI) [24], [25], has been used to estimate the differential ionospheric phase $\phi_{\text{ion},d}$ in regular InSAR interferograms.

Estimating ionosphere using range split-spectrum method for InSAR was proposed in [15], [16] and well demonstrated in [18]. We apply this method to ScanSAR. Using this method, the differential ionospheric phase $\phi_{\text{ion},d}$ to be removed from interferogram can be given by

$$\phi_{\text{ion},d} = \frac{f_l f_u}{f_0 (f_u^2 - f_l^2)} (\phi_l f_u - \phi_u f_l) \tag{14}$$

where f_0 is the radar carrier frequency, f_l is the center frequency of the lower band, f_u is the center frequency of the upper band, ϕ_l is the interferometric phase of the lower band, and ϕ_u is the interferometric phase of the upper band. The azimuth derivative of the resulting differential ionospheric phase $\phi_{\text{ion},d}$ can be used to mitigate the relative azimuth shift caused by ionosphere.

After getting the differential ionospheric phase $\phi_{\text{ion},d}$, ionospheric correction can be performed on the MAI interferogram. According to equation (8) and equation (13), the relationship between the MAI phase ϕ_{MAI} and the azimuth derivative of differential ionospheric phase $\partial\phi_{\text{ion},d}/\partial\eta$ is

$$\phi_{\mathrm{MAI}} = -\frac{nT_C}{2} \cdot \frac{\partial \phi_{\mathrm{ion},d}}{\partial \eta} \tag{15}$$

This *exact* (No regression based on real data processing is required for estimating $-nT_C/2$ in equation (15)) relationship is validated by our real data processing. Note this exact relationship is *not varying in range*.

C. Error Analysis

Two error sources can contribute to the error of the final azimuth deformation measurement. The first one is the phase noise in the MAI interferogram. According to equation (8), standard deviation of the azimuth deformation can be given by

$$\sigma_x = \frac{v_g}{2\pi n K_a T_C} \sigma_{\phi_{\mathrm{MAI}}} \tag{16}$$

where $\sigma_{\phi_{\mathrm{MAI}}}$ is the phase standard deviation of the MAI interferogram, which can be given by

$$\sigma_{\phi_{\mathrm{MAI}}} = \sqrt{\sigma_{\phi_1}^2 + \sigma_{\phi_2}^2} \tag{17}$$

where σ_{ϕ_1} and σ_{ϕ_2} are the phase standard deviations of the two bursts used to form MAI interferogram. Here, we have assumed the two burst interferograms are independent, which is the case for ScanSAR as the azimuth burst spectra do not overlap. The phase standard deviation of a spatially averaged interferogram is [1], [26]

$$\sigma_\phi = \frac{1}{\sqrt{2N}} \frac{\sqrt{1-\gamma^2}}{\gamma} \tag{18}$$

where γ is the coherence, and N is the number of resolution elements. N should be large enough to make equation (18) valid.

The other error source is the error of the azimuth derivative of the differential ionospheric phase. In the implementation, azimuth derivative can be performed by subtraction. It's reasonable for us to assume the random noises of the two resolution elements are independent. Therefore, according to equation (13), the standard deviation of the relative azimuth shift calculated using azimuth derivative of the differential ionospheric phase is

$$\sigma_{x_{\mathrm{ion},d}} = \frac{v_g}{K_a} \cdot \frac{1}{4\pi} \cdot \frac{1}{\Delta\eta} \cdot \sqrt{\sigma_{\phi_{\mathrm{ion},d,i+1}}^2 + \sigma_{\phi_{\mathrm{ion},d,i}}^2} \tag{19}$$

where i is the azimuth line number, $\Delta\eta$ is the azimuth time interval between two adjacent lines, and $\sigma_{\phi_{\mathrm{ion},d}}$ is the standard deviation of the differential ionospheric phase $\phi_{\mathrm{ion},d}$, which can be given by

$$\sigma_{\phi_{\mathrm{ion},d}} = \frac{f_l f_u}{f_0 (f_u^2 - f_l^2)} \sqrt{f_u^2 \sigma_{\phi_l}^2 + f_l^2 \sigma_{\phi_u}^2} \tag{20}$$

where σ_{ϕ_l} and σ_{ϕ_u} are the phase standard deviations of the lower and upper band interferograms, which can be given by equation (18).

We present the numerical results using parameters from the ALOS-2 ScanSAR data acquired over Nepal on Feb. 22, 2015. This is WBD mode (ScanSAR nominal [14MHz] mode Dual polarization) [27]. There are five subswaths, and we use

parameters from subswath 3. When a range varying parameter is required, we use its value at the center of subswath 3. We assume the coherences of the two look interferograms are the same. The standard deviation of the azimuth deformation σ_x given by equation (16) is shown in Fig. 2. The number of looks of the ScanSAR system is about five. The maximum burst number difference n is therefore four. We have used $n = 3$ to calculate the results shown in Fig. 2. For real data processing, a realistic value of N is 37 which is the one we use in our data processing. Note that the accuracy of the final result can be improved by averaging results of different n values as the number of looks of the ScanSAR system is about five.

If full aperture is used, the azimuth resolution of the differential ionospheric phase $\phi_{\mathrm{ion},d}$ estimated by range split-spectrum method is full aperture length (Actual resolution may be better than this due to the antenna pattern and the weighting applied in the focusing). It is reasonable to average a large number of samples in the azimuth direction, which results in an azimuth sample size comparable to the azimuth resolution of $\phi_{\mathrm{ion},d}$. In the meantime, we also make the slant range sample size equal to azimuth sample size along the orbit. This leads to relatively large N. We then calculate the standard deviation of the relative azimuth shift $\sigma_{x_{\mathrm{ion},d}}$ given in equation (19) according to different azimuth sample sizes (corresponding to different N values). The range split-spectrum scheme suggested in [1], [16] is used. We assume all the coherences involved are the same. The result is shown in Fig. 3, where we use fraction of full-aperture length to denote the resulting azimuth sample size. From Fig. 3, we can see that mitigating the relative azimuth shift using the differential ionospheric phase estimated using the range split-spectrum method is possible for ALOS-2 ScanSAR data.

D. Limitation

From real data processing, we find the resolution of the relative azimuth shift measured by the MAI interferogram is actually better than that calculated from the differential ionospheric phase estimated using range split-spectrum method. Furthermore, filtering is usually required to reduce random noise. As noticed in [18], while filtering can reduce random noise to a very low level, it also causes bias especially in the low coherence areas where larger filtering window is required to get a smoother result. Considering these two factors, the relative azimuth shift calculated is a biased result if the relative azimuth shift appearing in the MAI interferogram varies quickly.

Two solutions can be considered. First, if the coherence is high, we can reduce the azimuth aperture in the data processing of the range split-spectrum method to improve the resolution of the estimated differential ionospheric phase $\phi_{\mathrm{ion},d}$. For a multiple look ScanSAR system, we can use a number of looks that is smaller than the number of looks of the system. Second, we can choose an InSAR pair whose relative azimuth shift does not vary very quickly. This is possible with L-band data as temporal decorrelation is not as strong as other data acquired at shorter wavelengths, such as C-band. Therefore, many more acquisitions are available for interferometry. This is indeed the case for ALOS-2 considering other factors affecting coherence such as baseline and burst overlap are well under control.

III. From ALOS-2 Full-aperture ScanSAR Product to Burst-by-burst Interferometric Processing

A. Extracting Bursts from ALOS-2 Full-aperture ScanSAR Product

The ALOS-2 full-aperture ScanSAR product is focused using a stripmap focusing algorithm after filling burst gaps with zero echoes [11]. As a result, the focused image is a stripmap-like image, and individual bursts are no longer available. Furthermore, important parameters such as burst length, burst gap length and start times of raw bursts, are not available from the product either. These parameters are required as input before retrieving individual bursts from full-aperture product. We estimate these parameters using methods described in [28].

The burst signal of a target after focusing can be expressed as [20]

$$s_f(\eta) = T_B \mathrm{sinc}(K_a T_B \eta) \cdot \exp\{j\pi K_a \eta(\eta - 2\eta_c)\} \tag{21}$$

where T_B is the burst length, η is the azimuth time, η_c is the offset between the target's zero Doppler time and burst center, and K_a ($K_a > 0$) is the azimuth FM rate. We have ignored the range of closest approach, the antenna pattern, the weighting applied in the focusing and the complex constant modeling the backscattering characteristic. The time-frequency plot of a multiple look ScanSAR system is shown in Fig. 4(a). For full-aperture image, signals from different bursts are superimposed. Supposing that we are going to extract burst B_4 as shown in Fig. 4 from full-aperture image, we determine the imaged area of burst B_4 (azimuth range between the two vertical dashed lines in Fig. 4) using the start time of raw burst B_4 and Doppler centroid frequency. Then the corresponding bulk of image, which also contains signals from other bursts (B_1-B_3 and B_5-B_7), is read into memory and multiplied by

$$p(\eta) = \exp\{-j\pi K_a(\eta + \eta_{\mathrm{offset}})^2\} \tag{22}$$

where η_{offset} is the offset between the center of $p(\eta)$ and the center of the focused burst to be extracted. Now the azimuth-varying spectrum of each burst is moved to a limited band as shown in Fig. 4(b). In Fig. 4(b), to make it clearer, we have assumed a much longer $p(\eta)$, and other bursts involved (B_1-B_3 and B_5-B_7) are also fully multiplied by it. Depending on different η_{offset} values, the resulting azimuth signal of each burst can be baseband signal or non-baseband signal. In our implementation, we choose a η_{offset} value that moves the spectrum of burst B_4 to a baseband. We then use a bandpass filter to capture the spectrum of burst B_4 as shown in Fig. 4(c). Now the azimuth sampling rate is still PRF, which is much larger than azimuth burst bandwidth. Therefore, we downsample the filtered burst according to the desired oversampling ratio to reduce data volume. Finally, the downsampled burst is multiplied by the conjugate of equation (22), and the spectrum is moved back as shown in Fig. 4(d). Other bursts can be extracted exactly in the same way.

In the above discussion, we have only extracted the targets that are fully imaged by a burst. Also, we have used full azimuth spectrum (corresponding to PRF), which is actually possible with ALOS-2 as full azimuth spectrum is kept during focusing. In practice, we usually use only a fraction (e.g. 90%) of the full azimuth spectrum to remove the darker samples with lower signal-to-noise ratio (SNR) on burst edges. For ALOS-2, the availability of full azimuth spectrum is a benefit of extracting bursts from full-aperture product as we can determine how much azimuth spectrum we want to use by ourselves. On the other hand, not all azimuth spectrum is kept in the burst-by-burst product.

In the extraction of bursts, an important problem is whether we should consider the aliasing effect after multiplying the image by equation (22). That is, whether we

should consider the possibility that burst signals may overlap. We can understand this problem in this way. In Fig. 4(b), there are two dimensions: the azimuth dimension and the frequency dimension. In azimuth dimension, spectrum of different bursts may overlap (e.g. burst B_2 and B_5). In frequency dimension, at each azimuth location, multiplying by equation (22) just moves the whole azimuth spectrum and relative locations of different burst spectra remain the same. In other words, different burst spectra never overlap in this dimension. For burst extraction, each target imaged by burst B_4 is extracted at its own azimuth location. In this case, azimuth dimension is fixed, and we only have to consider frequency dimension. Therefore, we never have to consider the problem that burst signals may overlap. However, in the estimation of burst parameters (e.g. burst length, burst gap length and start times of raw bursts), the problem should be properly considered, as many azimuth targets are involved, and azimuth dimension is not fixed [28].

An example of burst extraction is shown in Fig. 5.

B. Removal of Azimuth Non-overlap Spectra

Azimuth non-overlap spectra are caused by Doppler centroid frequency difference and burst misalignment. For this particular case, three methods are possible to remove azimuth non-overlap spectra. The first method is to filter the full-aperture image using a multi-band bandpass filter [28] before extracting bursts. The second method is to filter the extracted bursts using a bandpass filter as done in the regular burst-by-burst processing.

For our implementation, we remove azimuth non-overlap spectra by adjusting burst parameters when extracting bursts according to Doppler centroid frequency difference and burst misalignment. To remove non-overlap spectrum caused by burst misalignment, we need to change burst length for both acquisitions and burst start times of the acquisition whose bursts are in front of the corresponding bursts of the other acquisition. Doppler centroid frequency difference reduces the full azimuth spectrum available for interferometry. Non-overlap spectrum caused by Doppler centroid frequency difference is actually not necessarily to be removed, as it is spectrum of targets in the non-overlap area of a burst pair. Removing azimuth non-overlap spectra by adjusting burst parameters is a computationally efficient way as no extra computation is required. A comparison of burst interferograms generated using bursts without and with the removal of azimuth non-overlap spectra is shown in Fig. 5. Compared with Fig. 5(c), there is less noise in Fig. 5(d), which indicates the successful removal of azimuth non-overlap spectra.

C. Coregistration

For the coregistration of burst-by-burst ScanSAR InSAR processing, the commonly accepted method is geometric coregistration [29] followed by a spectral diversity coregistration [4]. For ALOS-2, we find that even after geometric coregistration, there is still significant residual coregistration error which is probably caused by inaccurate geometry and recent strong ionosphere. In particular, the residual error may even cause complete loss of coherence, and therefore spectral diversity cannot be performed any more.

To coregister the InSAR pair for regular InSAR processing, we first coregister the pair using geometric coregistration. The slave bursts are resampled according to the geometric coregistration offsets. The master bursts and coregistered slave bursts are used to form a pair of amplitude images, on which a cross-correlation coregistration is

performed. Both range and azimuth coregistration offsets can be refined by polynomials fitted to the cross-correlation coregistration offsets. Now burst interferograms with good coherence can be formed, and spectral diversity can be done to further improve azimuth offsets. Using the final range and azimuth offsets, we resample slave bursts for the third time to form the final burst interferograms. The whole coregistration flow is shown in Fig. 6.

Some changes can be made to this coregistration flow in order to measure azimuth deformation, which will be discussed in Section V.

A comparison of interferograms processed using full-aperture approach and burst-by-burst approach is shown in Fig. 7. The two results should be generally the same [30]. In the difference of the two interferograms shown in Fig. 7(c), there are some small areas with bigger differences. A possible reason for this is that these areas are mostly areas with very low amplitudes as shown in Fig. 7(d), and therefore the SNRs of these areas are very low.

IV. Ionosphere Estimation for ScanSAR Interferometry

We apply the range split-spectrum method [15], [16], [18] to ScanSAR to estimate the differential ionospheric phase $\phi_{\mathrm{ion},d}$ in ScanSAR interferogram. In the generation of subband image, we need to be careful if the center frequency is moved back to zero. According to the property of Fourier Transform,

$$g(t) \cdot \exp\{j2\pi f_c t\} \leftrightarrow G(f - f_c) \tag{23}$$

where t is the time, f is the frequency, f_c is the amount of frequency to be shifted, $g(t)$ is the original time-domain function, and $G(f - f_c)$ is the frequency domain function after frequency shifting. Suppose that the linear phase to be multiplied is

$$l(t) = 2\pi f_c t. \tag{24}$$

For ScanSAR, the range time t in equation (24) should have the same origin for all subswaths to make the differential ionospheric phase estimates consistent for all subswaths. If there is a relative range time error t_ϵ between the subswaths of an acquisition as shown in Fig. 8, it will cause phase errors to subband interferograms and eventually propagate to the differential ionospheric phase $\phi_{\mathrm{ion},d}$ in equation (14). Note that for the same relative range time error t_ϵ, the phase error caused to the lower and upper band interferograms are different as their center frequencies in equation (24) are different. Therefore, unlike the common phase unwrapping error of two subband interferograms that has a little effect [18], the different phase errors of the lower and upper band interferograms caused by the same t_ϵ can have a big effect in the resulting differential ionospheric phase. The total phase error caused will be

$$\phi_{\mathrm{ion},d;\epsilon} = \frac{4\pi f_l^2 f_u^2}{f_0(f_u^2 - f_l^2)} t_\epsilon \tag{25}$$

We evaluate the relative accuracy requirement of range time for ALOS-2 WBD mode (wavelength: 0.242 m. nominal range bandwith: 14 MHz. actual range bandwith: 11899999.8 Hz). If the range split-spectrum scheme suggested in [1], [16] is used and $\phi_{\mathrm{ion},d;\epsilon} \leq 0.1$ rad, this requires that the relative range time error is less than or equal to 2.88×10^{-6} range sample.

We choose to move the center frequency to zero after range filtering in order to use our original InSAR processor in range split-spectrum method without any changes. The subswath range starting time of ALOS-2 product is far from meeting the relative accuracy requirement of range time. To solve the problem, we first coregister the subswaths using amplitude images to do a correction, which removes the majority of relative range time error. We then compensate for the relative phase error of subswath interferograms caused by the remaining relative range time error using the phase difference in the overlap area between adjacent subswaths. When mosaicking consecutive frames, similar problem exists. The same solution can also be applied to this case. A comparison of the different estimates of the differential ionospheric phase after filtering is shown in Fig. 9.

The estimated differential ionospheric phase and its azimuth derivative can be used to correct the InSAR and MAI interferograms, respectively. Here, we present ionospheric correction examples for ALOS-2 ScanSAR interferometry. Fig. 10 shows the ionospheric correction result for April 25, 2015 *Mw*7.8 Nepal earthquake. For this InSAR pair, the frame numbers of the data we have are slightly different. In addition, incomplete bursts on image edges are not extracted. These make the resulting interferogram smaller in azimuth. The same InSAR pair and several other pairs were processed by E. O. Lindsey *et al.* [31] and us shortly after the earthquake, but without appropriate ionospheric correction. Fig. 11 shows the ionospheric correction result for September 16, 2015 *Mw*8.3 Chile earthquake. For this result, we processed three consecutive frames, and the total covered area is about 360×810 km^2 (range×azimuth). The original interferogram shows strong differential ionospheric phase in a large scale. The corrected interferogram is compared with Sentinel-1A TOPS interferogram of the same area processed by us. To compare the two results, the Sentinel-1A interferogram is filtered, unwrapped and scaled according to the ratio of ALOS-2 and Sentinel-1A wavelengths.

V. Measuring Azimuth Deformation

A. MAI Interferogram Formation

For the purpose of measuring azimuth deformation, the coregistration flow presented in section III-C needs some changes. In the azimuth direction, the offset between the InSAR pair can be expressed as

$$x = x_{\text{def}} + x_{\text{ion},d} + x_{\text{geo}} \tag{26}$$

where x_{def} is the offset caused by azimuth deformation of the ground, $x_{\text{ion},d}$ is the relative azimuth shift caused by ionosphere, and x_{geo} is the offset caused by geometric difference. All of these offsets contribute to the azimuth deformation measured by MAI. For the coregistration, the first step is still geometric coregistration without any change. This step removes the spatially varying part of x_{geo} and leaves only the constant part of x_{geo}. After this step, the offset between the InSAR pair is

$$x = x_{\text{def}} + x_{\text{ion},d} + x_{\text{geo,const}} \tag{27}$$

where $x_{\text{geo,const}}$ is the remaining constant part of x_{geo}. According to our experience, $x_{\text{geo,const}}$ can be bigger than one sample in both range and azimuth (1/PRF). While the azimuth $x_{\text{geo,const}}$ may not cause significant coherence loss as the azimuth resolution is much coarser, the range $x_{\text{geo,const}}$ may lead to complete decorrelation.

The next step is cross-correlation coregistration. This step is mainly for recovering coherence. As in section III-C, a polynomial can be fitted to the range cross-correlation coregistration offsets to remove the majority of the remaining range mis-registration. In azimuth, a linear or higher order polynomial fitted to the azimuth cross-correlation coregistration offsets is not appropriate, as the resulting spatially varying signatures will be mixed with those of $x_{\mathrm{ion},d}$. This will cause problems in the following steps. Instead, we should take the average of the azimuth cross-correlation coregistration offsets, and use it to refine the azimuth offset. After this step, azimuth offset is

$$x = x_{\mathrm{def}} + x_{\mathrm{ion},d} + \left(x_{\mathrm{geo,const}} - x_{\mathrm{cc,const}}\right) = x_{\mathrm{def}} + x_{\mathrm{ion},d} + x_{\mathrm{const}} \tag{28}$$

where $x_{\mathrm{cc,const}}$ is the average of the azimuth cross-correlation coregistration offsets, and $x_{\mathrm{const}} = x_{\mathrm{geo,const}} - x_{\mathrm{cc,const}}$ which is a constant.

Now burst interferograms with high coherence can be formed. For ALOS-2 WBD mode, the number of looks is about five. Thus, we can form five continuous interferograms using the burst interferograms. Each interferogram represents a look. The time span between adjacent looks is T_C. Now four MAI interferograms, with different n values as shown in equation (8), can be formed using the five interferograms. This is done for each subswath. For each look, the subswath MAI interferograms are mosaicked to form the whole swath MAI interferograms. In the mosaicking, while $x_{\mathrm{def}} + x_{\mathrm{ion},d}$ is consistent for different subswaths in equation (28), x_{const} is not necessarily the same (For ALOS-2, x_{geo} is different for different subswaths. $x_{\mathrm{cc,const}}$ is also different for different subswaths, as it is obtained from cross-correlation of amplitude images of each subswath.). The azimuth offset difference between adjacent subswaths is thus a constant and can be given by

$$x_d = x_{\mathrm{const},s} - x_{\mathrm{const},s+1} \tag{29}$$

where s and $s+1$ indicate the subswath numbers. We then adjust the phase of one of the subswath MAI interferograms using the average value of the phase difference in the overlap area between the adjacent subswaths. After mosaicking, for each whole swath MAI interferogram, the azimuth offset can be given by

$$x = x_{\mathrm{def}} + x_{\mathrm{ion},d} + x_{\mathrm{const,adj}} \tag{30}$$

where $x_{\mathrm{const,adj}}$ is the x_{const} of the whole swath after adjustment, and is still a constant. Each whole swath MAI interferogram is filtered by the adaptive power-spectrum filter [32] to suppress random noise caused by decorrelation. The filtered interferograms are then unwrapped by snaphu [33].

B. Phase Correction of the MAI Interferograms

To remove the phase caused by $x_{\mathrm{ion},d}$ and $x_{\mathrm{const,adj}}$ from the MAI interferogram, we mask out the area with azimuth deformation of the ground x_{def}. In the remaining area, the azimuth offset is thus

$$x = x_{\mathrm{ion},d} + x_{\mathrm{const,adj}} \tag{31}$$

With the azimuth derivative of the differential ionospheric phase $\partial\phi_{\mathrm{ion},d}/\partial\eta$ available from section IV, two methods can be used to correct for the phase caused by $x_{\mathrm{ion},d}$ and $x_{\mathrm{const,adj}}$. The first method is to convert $\partial\phi_{\mathrm{ion},d}/\partial\eta$ to MAI interferogram phase $\phi_{\mathrm{MAI;ion},d}$ using equation (15), and subtract it from the MAI interferogram. The

remaining phase of the MAI interferogram is mainly caused by $x_{\text{const,adj}}$. We then take the average of the remaining phase, which is denoted as $\phi_{\text{MAI;const,adj}}$. $\phi_{\text{MAI;ion},d}$ and $\phi_{\text{MAI;const,adj}}$ are removed from the original MAI interferogram without mask to get the corrected MAI interferogram. As the second method, we can do a simple linear polynomial fit between $\partial\phi_{\text{ion},d}/\partial\eta$ and the phase ϕ_{MAI} of the MAI interferogram using all available samples, as they are linearly proportional and their relationship is not range or azimuth variant. To correct for the phase caused by $x_{\text{ion},d}$ and $x_{\text{const,adj}}$, the following phase is removed from the original MAI interferogram without mask

$$\phi_{\text{fit}} = a\frac{\partial\phi_{\text{ion},d}}{\partial\eta} + b \tag{32}$$

where a and b are the coefficients of the polynomial, and a represents the relationship given by equation (15) and b represents the phase caused by $x_{\text{const,adj}}$. Phase correction is done for each MAI interferogram.

C. Azimuth Deformation

Now theoretically each MAI interferogram only contains phase caused by azimuth deformation of the ground. The phase of each MAI interferogram is converted to azimuth deformation according to equation (8). The final azimuth deformation is the weighting average of all deformations.

All the methods are implemented as additions to ISCE [34].

VI. Results

In the previous sections, two pairs of ALOS-2 WBD mode data are used: the Nepal pair acquired on Feb. 22, 2015 and May 3, 2015, and the Chile pair acquired on Jul. 30, 2015 and Sep. 24, 2015. In this section, we take the Nepal pair as an example to demonstrate azimuth deformation measurement. For this pair, we find anomaly in subswath 2. But subswaths 3, 4 and 5 are enough for covering the azimuth deformation caused by April 25, 2015 *Mw*7.8 Nepal earthquake. Therefore, the three subswaths are processed.

The MAI interferograms without phase correction are presented in Fig. 12. As we can see from this figure, the MAI phase is more and more obvious as the time span of the two look interferograms used to form the MAI interferogram becomes bigger. The phase caused by the azimuth deformation of Nepal earthquake is very clear. In the meantime, the phase caused by $x_{\text{ion},d}$ and $x_{\text{const,adj}}$ as given in equation (30) is also very strong.

The azimuth derivative of the differential ionospheric phase estimated using range split-spectrum method is shown in Fig. 13. Each of the two methods mentioned in Section V-B can be used to correct the phase of the MAI Interferograms. Before doing this, we first validate the exact relationship between the MAI phase ϕ_{MAI} and the azimuth derivative of differential ionospheric phase $\partial\phi_{\text{ion},d}/\partial\eta$ given by equation (15). This is a critical validation of the systematic analysis of Section II. The coefficient $-nT_C/2$ in equation (15) should be equal to the polynomial coefficient a in equation (32). $-nT_C/2$ is calculated using the relating parameters, while a is estimated in polynomial fitting. The results are given in Table I. From this table, we

can see that the two values are very close to each other. The difference is mainly caused by the bias in $\partial\phi_{\mathrm{ion},d}/\partial\eta$, which affects the coefficients of the polynomial.

After phase correction, the MAI interferograms are shown in Fig. 14. Most of the phase caused by $x_{\mathrm{ion},d}$ and $x_{\mathrm{const,adj}}$ is removed from each MAI interferogram. However, there are still residuals. As discussed in Section II-D, this is mainly caused by the bias in $\partial\phi_{\mathrm{ion},d}/\partial\eta$. This is actually the major error, which outweighs the random error. It is difficult to quantitatively assess the error caused by the bias.

The final azimuth deformation is shown in Fig. 15(a). The maximum deformation caused by Nepal earthquake is up to 2.6 m. To validate this result, we estimate the azimuth deformation by incoherent cross correlation using a pair of high resolution RADARSAT-2 images. The azimuth ground pixel size of the Radarsat-2 images is about 2.50 m. The images cover half of the deformation area. The result of incoherent cross correlation is shown in Fig. 15 (b). This result has been used in the modeling of this earthquake [35]. The difference between the two results is shown in Fig. 15 (c). We can see from this figure that there is no big difference between the two results. We also wrap the final azimuth deformation and put it on optical image to show the deformation area, which is shown in Fig. 16. Because of the shallow (roughly 5°) dip and depth greater than 10 km of the Main Himalayan Thrust (MHT) that slipped during the Gorkha Earthquake [35], the northward motion of the footwall block below the fault is not visible at the surface. Therefore, all the deformation measured in Fig. 16 is positive, which is very different from the range deformation measured using regular InSAR.

VII. Conclusion

We show the possibility of measuring azimuth deformation with L-band ALOS-2 ScanSAR interferometry. In the theoretical analysis, how MAI and spectral diversity correspond to each other is clearly explained. The *exact* relationship between the MAI phase and the azimuth derivative of differential ionospheric phase is given and subsequently validated by real data processing. Error analysis shows that mitigating the relative azimuth shift using the differential ionospheric phase estimated using the range split-spectrum method is possible for ALOS-2 ScanSAR data. The major limitation is the bias in the relative azimuth shift calculated from the estimated differential ionospheric phase.

In the implementation, we show that it is possible to process ALOS-2 full-aperture ScanSAR product using a burst-by-burst interferometric processing approach. The range split-spectrum method is successfully applied to ScanSAR to estimate the differential ionospheric phase in ScanSAR interferogram, and the azimuth derivative of the estimated differential ionospheric phase can be used to mitigate the relative azimuth shift caused by ionosphere in the MAI interferogram. By properly processing the data, it is possible to separate the phase caused by azimuth deformation of the ground from the phase of the MAI interferogram consisting of phases caused by azimuth deformation of the ground, relative azimuth shift caused by ionosphere, and geometric difference.

There is no big difference between the interferograms processed by full-aperture approach and burst-by-burst approach. Experience with processing a large amount of data shows that the recent interferograms are strongly affect by ionosphere, and examples of strong large-scale differential ionospheric phase appearing in ALOS-2

ScanSAR interferogram are shown in this paper. The large-scale azimuth deformation caused by Nepal earthquake is measured by ALOS-2 ScanSAR Interferometry, and the result is in agreement with azimuth deformation measured by incoherent cross correlation using a pair of high resolution RADARSAT-2 images. Our result shows that the maximum azimuth deformation caused by Nepal earthquake is up to 2.7 m. These also provide implications for the NASA's NISAR mission and future NASA spaceborne SAR missions.

Acknowledgment

This research was carried out at the Jet Propulsion Laboratory (JPL), California Institute of Technology, under a contract with the National Aeronautics and Space Administration (NASA Earth Surface and Interior focus area). This research was also supported by an appointment to the NASA Postdoctoral Program at JPL. The ALOS-2 original data are copyright Japan Aerospace Exploration Agency (JAXA) and provided under JAXA RA4 PI projects P1372002 and P1385002. The Sentinel-1A interferogram contains modified Copernicus Sentinel data [2015]. Original RADARSAT-2 data and products are copyright 2015 McDonald, Dettweiler and Associates Ltd (MDA)–all rights reserved. RADARSAT is an official trademark of the Canadian Space Agency (CSA). RADARSAT-2 data products were provided under the CSA Science and Operational Applications Research and development program (SOAR) Geohazard Project number 5320. We thank our colleagues Paul A. Rosen for his early development of the range split-spectrum method for ionospheric correction and Piyush Agram for useful discussions and his geometrical coregistration programs. We thank Ryo Natsuaki (JAXA) for discussions about ALOS-2 product and Franz J. Meyer (University of Alaska Fairbanks) for discussions about ionosphere. We also thank the reviewers for their comments that improved this paper.

References

[1] R. Bamler and M. Eineder, "Accuracy of differential shift estimation by correlation and split-bandwidth interferometry for wideband and Delta-k SAR systems," *IEEE Geosci. Remote Sens. Lett.*, vol. 2, no. 2, pp. 151-155, Apr. 2005.

[2] R. Michel, J.-P. Avouac, and J. Taboury, "Measuring ground displacements from SAR amplitude images: Application to the Landers Earthquake," *Geophys. Res. Lett.*, vol. 26, no. 7, pp. 875-878, Apr. 1999.

[3] N. B. D. Bechor and H. A. Zebker, "Measuring two-dimensional movements using a single InSAR pair," *Geophys. Res. Lett.*, vol. 33, no. 16, pp. L16311, Aug. 2006.

[4] R. Scheiber and A. Moreira, "Coregistration of interferometric SAR images using spectral diversity," *IEEE Trans. Geosci. Remote Sens.*, vol. 38, no. 5, pp. 2179–2191, Sep. 2000.

[5] H. Jung, Z. Lu, A. Shepherd, and T.Wright, "Simulation of the SuperSAR multi-azimuth synthetic aperture radar imaging system for precise measurement of three-dimensional Earth surface displacement," *IEEE Trans. Geosci. Remote Sens.*, vol. 53, no. 11, pp. 6196–6206, Nov. 2015.

[6] K. Tomiyasu, "Conceptual performance of a satellite borne, wide swath synthetic aperture radar," *IEEE Trans. Geosci. Remote Sens.*, vol. GE-19, no. 2, pp. 108–116, Apr. 1981.

[7] R. K. Moore, J. P. Claassen, and Y. H. Lin, "Scanning spaceborne synthetic aperture radar with integrated radiometer," *IEEE Trans. Aerosp. Electron. Syst.*, vol. AES-17, no. 3, pp. 410–420, May 1981.
[8] A. Monti Guarnieri and C. Prati, "ScanSAR focusing and interferometry," *IEEE Trans. Geosci. Remote Sens.*, vol. 34, no. 4, pp. 1029–1038, July 1996.
[9] Y. Kankaku, Y. Osawa, S. Suzuki, and T. Watanabe, "The overview of the L-band SAR onboard ALOS-2," in *Proc. PIERS*, Moscow, Russia, Aug. 18–21, 2009, pp. 735–738.
[10] Y. Kankaku, "ALOS-2 and PALSAR-2 development status," presented in *Cal-Val Science Team (CVST) Meeting*.
[11] R. Bamler and M. Eineder, "ScanSAR processing using standard high precision SAR algorithms," *IEEE Trans. Geosci. Remote Sens.*, vol. 34, no. 1, pp. 212–218, Jan. 1996.
[12] F. Meyer, R. Bamler, N. Jakowski, and T. Fritz, "The potential of low-frequency SAR systems for mapping ionospheric TEC distributions," *IEEE Geosci. Remote Sens. Lett.*, vol. 3, no. 4, pp. 560-564, Oct. 2006.
[13] F. J. Meyer, "Performance requirements for ionospheric correction of low-frequency SAR data," *IEEE Trans. Geosci. Remote Sens.*, vol. 49, no. 10, pp. 3694–3702, Oct. 2011.
[14] Z. Liu, H.-S. Jung, and Z. Lu, "Joint correction of ionosphere noise and orbital error in L-Band SAR interferometry of interseismic deformation in southern California," *IEEE Trans. Geosci. Remote Sens.*, vol. 52, no. 6, pp. 3421– 3427, Jun. 2014.
[15] P. A. Rosen, S. Hensley, and C. Chen, "Measurement and mitigation of the ionosphere in L-band interferometric SAR data," in *Proc. 2010 IEEE Radar Conference*, Washington, DC, USA, May 10-14, 2010, pp. 1459 – 1463.
[16] R. Brcic, A. Parizzi, M. Eineder, R. Bamler, and F. Meyer, "Estimation and compensation of ionospheric delay for SAR interferometry," in *Proc. 2010 IEEE IGARSS*, Honolulu, HI, USA, Jul. 25-30, 2010, pp. 2908 – 2911.
[17] P. A. Rosen, S. Hensley, S. Shaffer, L. Veilleux, M. Chakraborty, T. Misra, R. Bhan, V. Raju Sagi, and R. Satish, "The NASA-ISRO SAR mission - An international space partnership for science and societal benefit," in *Proc. 2015 IEEE Radar Conference*, Arlington, VA, USA, May 10-15, 2015, pp. 1610 - 1613.
[18] G. Gomba, A. Parizzi, F. De Zan, M. Eineder, and R. Bamler, "Toward operational compensation of ionospheric effects in SAR interferograms: The split-spectrum method," *IEEE Trans. Geosci. Remote Sens.*, vol. 54, no. 3, pp. 1446 - 1461, Mar. 2016.
[19] R. Scheiber, M. Jäger, P. Prats-Iraola, F. De Zan, and D. Geudtner, "Speckle tracking and interferometric processing of TerraSAR-X TOPS data for mapping nonstationary scenarios," *IEEE J. Sel. Topics Appl. Earth Observ. Remote Sens.*, vol. 8, no. 4, pp. 1709–1720, Apr. 2015.
[20] I. G. Cumming and F. H. Wong, *Digital Processing of Synthetic Aperture Radar Data: Algorithms and Implementation*. Norwood, MA, USA: Artech House, 2005.
[21] R. F. Hanssen, *Radar interferometry: Data interpretation and error analysis*. Kluwer Academic Publishers, 2002.
[22] D. Raucoules and M. de Michele, "Assessing ionospheric influence on L-band SAR data: Implications on coseismic displacement measurements of the 2008

Sichuan earthquake," *IEEE Geosci. Remote Sens. Lett.*, vol. 7, no. 2, pp. 286-290, Apr. 2010.
[23] A. C. Chen and H. A. Zebker, "Reducing ionospheric effects in InSAR data using accurate coregistration," *IEEE Trans. Geosci. Remote Sens.*, vol. 52, no. 1, pp. 60-70, Jan. 2014.
[24] U. Wegmüller, T. Strozzi, and C. Werner, "Ionospheric path delay estimation using split-beam interferometry," in *Proc. 2012 IEEE IGARSS*, Munich, Germany, Jul. 22-27, 2012, pp. 3631-3634.
[25] H.-S. Jung, D.-T. Lee, Z. Lu, and J.-S. Won, "Ionospheric correction of SAR interferograms by multiple-aperture interferometry," *IEEE Trans. Geosci. Remote Sens.*, vol. 51, no. 5, pp. 3191-3199, May 2013.
[26] J. O. Hagberg, L. M. H. Ulander, and J. Askne, "Repeat-pass SAR interferometry over forested terrain," *IEEE Trans. Geosci. Remote Sens.*, vol. 33, no. 2, pp. 331-340, Mar. 1995.
[27] JAXA, *ALOS-2/PALSAR-2 level 1.1/1.5/2.1/3.1 CEOS SAR product format description*.
[28] C. Liang and E. J. Fielding, "Interferometry with ALOS-2 full-aperture ScanSAR data," *IEEE Trans. Geosci. Remote Sens.*, in press.
[29] E. Sansosti, P. Berardino, M. Manunta, F. Serafino, and G. Fornaro, "Geometrical SAR image registration," *IEEE Trans. Geosci. Remote Sens.*, vol. 44, no. 10, pp. 2861–2870, Oct. 2006.
[30] C. Liang, Q. Zeng, and J. Jiao, "An assessment of ScanSAR interferometric processing using full-aperture approach," *IEEE Geosci. Remote Sens. Lett.*, vol. 11, no. 9, pp. 1559-1563, Sep. 2014.
[31] E. O. Lindsey *et al.*, "Line of sight displacement from ALOS-2 interferometry: Mw 7.8 Gorkha earthquake and Mw 7.3 aftershock," *Geophys. Res. Lett.*, vol. 42, no. 16, pp. 6655–6661, Aug. 2015.
[32] R. M. Goldstein and C. L. Werner, "Radar interferogram filtering for geophysical applications," *Geophys. Res. Lett.*, vol. 25, no. 21, pp. 4035–4038, Nov. 1998.
[33] C. W. Chen and H. A. Zebker, "Two-dimensional phase unwrapping with use of statistical models for cost functions in nonlinear optimization," *J. Opt. Soc. Amer. A*, vol. 18, no. 2, pp. 338-351, Feb. 2001.
[34] P. A. Rosen, E. Gurrola, G. F. Sacco, and H. Zebker, "The InSAR scientific computing environment," in *Proc. EUSAR*, Nuremberg, Germany, Apr. 23–26, 2012, pp. 730–733.
[35] H. Yue *et al.*, "Depth varying rupture properties during the 2015 Mw 7.8 Gorkha (Nepal) earthquake," *Tectonophysics*, in press.

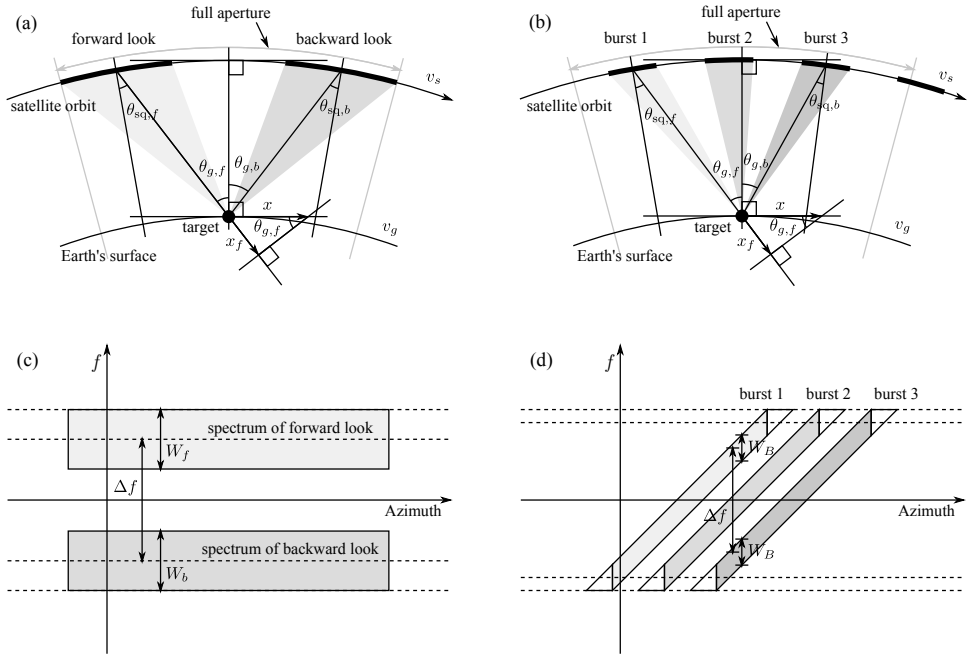

Fig. 1. (a) and (b) are stripmap and ScanSAR MAI geometries for a target in the slant range plane, respectively. (a) Stripmap. (b) 2-subswath 3-look ScanSAR system. The gray triangles represent the sweeping ranges of the radar line of sight with respect to the target on the ground. $\theta_{\mathrm{sq},f}$ and $\theta_{\mathrm{sq},b}$ are the actual squint angles along the orbit corresponding to the Doppler centroid frequencies of forward and backward looks, respectively. $\theta_{g,f}$ and $\theta_{g,b}$ are the squint angles on the ground corresponding to $\theta_{\mathrm{sq},f}$ and $\theta_{\mathrm{sq},b}$, respectively. The azimuth movement of the target on the ground is x, and the movement observed by forward look is x_f. v_s is the actual satellite velocity along the orbit, and v_g is the velocity of the beam footprint on the ground. (c) and (d) are stripmap and ScanSAR MAI spectra for multiple targets. (c) Stripmap. (d) 2-subswath 3-look ScanSAR system. The look spectra of (c) and (d) correspond to the look geometries in (a) and (b). W_f and W_b are the bandwidths of forward and backward looks in stripmap mode, W_B is the burst bandwidth in ScanSAR mode, and Δf is the frequency separation between the two looks.

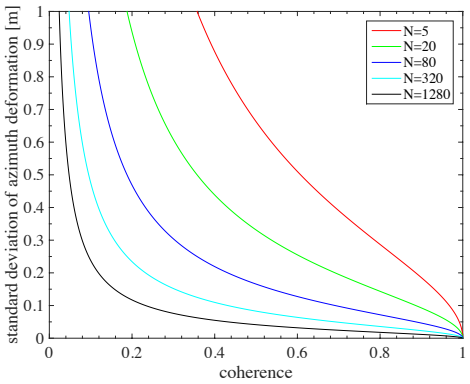

Fig. 2. The standard deviation of the azimuth deformation σ_x given by equation (16) for ALOS-2 WBD mode.

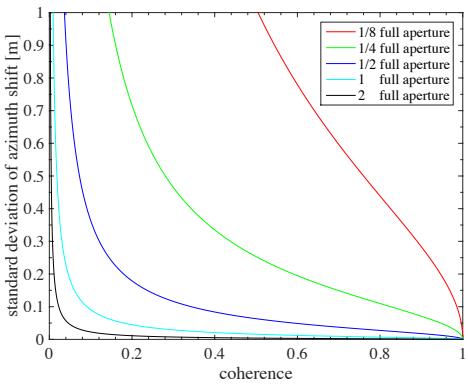

Fig. 3. The standard deviation of the relative azimuth shift $\sigma_{x_{\mathrm{ion},d}}$ given in equation (19) for ALOS-2 WBD mode. Fraction of full-aperture length is used to denote the resulting azimuth sample size of the relative azimuth shift calculated using azimuth derivative of the differential ionospheric phase.

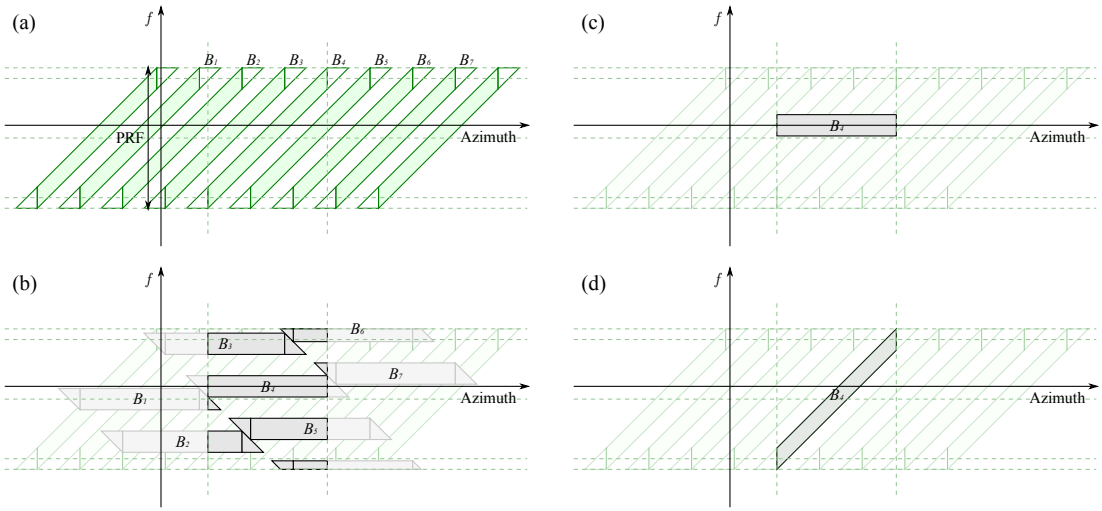

Fig. 4. Extracting bursts from full-aperture ScanSAR product. (a) Spectrum of full-aperture image. Burst B_4 is to be extracted. The azimuth range between the two vertical dashed lines are used in the extraction, and spectra of bursts B_1-B_3 and B_5-B_7 are involved in the extraction. Targets not fully imaged by burst B_4 are abandoned, and full azimuth spectrum (PRF) is used in the extraction. (b) Spectrum of full-aperture image multiplied by equation (22). Spectra of bursts B_1-B_3 and B_5-B_7 outside of the two vertical dashed lines are also shown as multiplied by equation (22) to make it clearer. (c) Bandpass filtering to extract burst B_4. (d) Moving the spectrum of extracted burst B_4 back. In (b), (c) and (d), spectrum of original full-aperture image is also plotted in light green as reference.

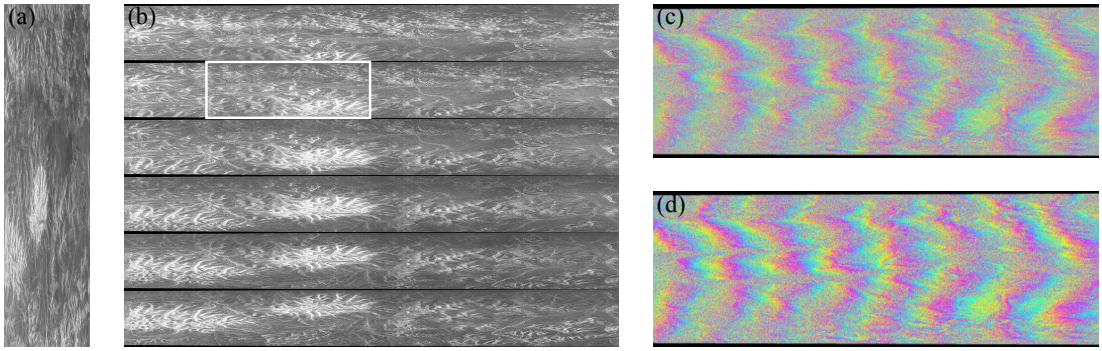

Fig. 5. (a) Full-aperture image from subswath 5 acquired on Feb. 22, 2015. (b) Extracted bursts. (c) and (d) are burst interferograms corresponding to the rectangle area. (c) Azimuth non-overlap spectra not removed. (d) Azimuth non-overlap spectra removed. The other image of the InSAR pair was acquired on May 3, 2015. Burst overlap: 74.7%.

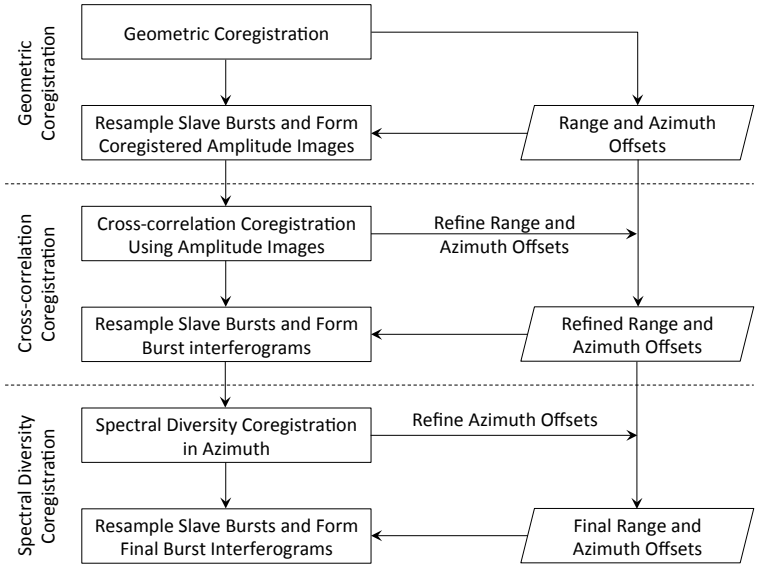

Fig. 6. Coregistration flow of ALOS-2 ScanSAR InSAR pair for regular burst-by-burst InSAR processing.

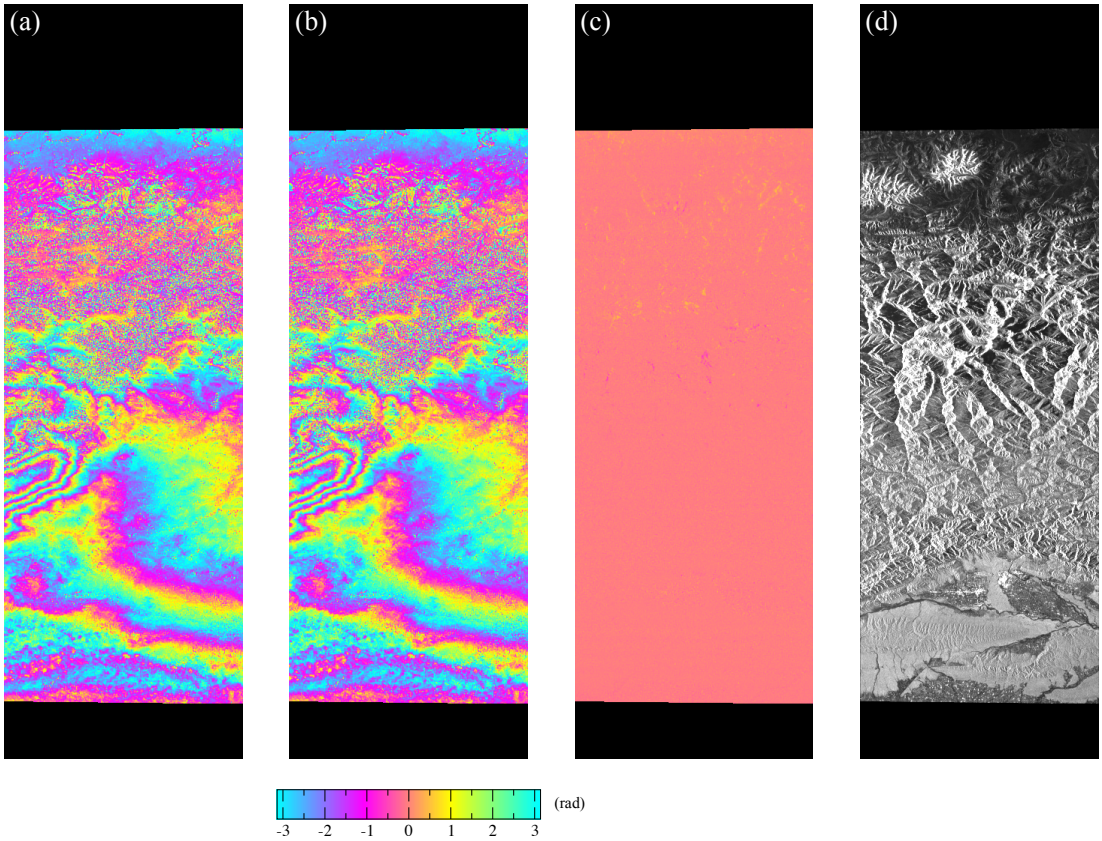

Fig. 7. A comparison of interferograms processed using burst-by-burst and full-aperture approaches. (a) Interferogram processed using burst-by-burst approach. (b) Interferogram processed using full-aperture approach. (c) Difference of the two interferograms. (d) Amplitude image of master from burst-by-burst processing. Data: subswath 5, Feb. 22, 2015 and May 3, 2015.

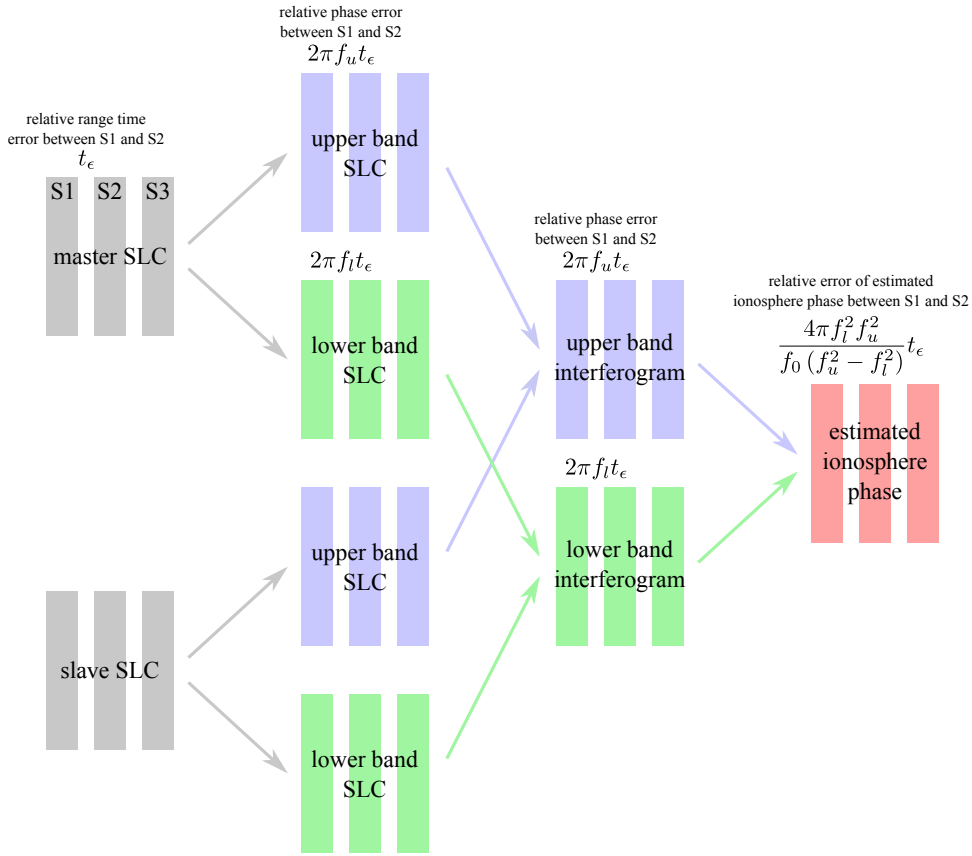

Fig. 8. The error propagation process for a relative range time error t_ϵ between the subswaths of an acquisition.

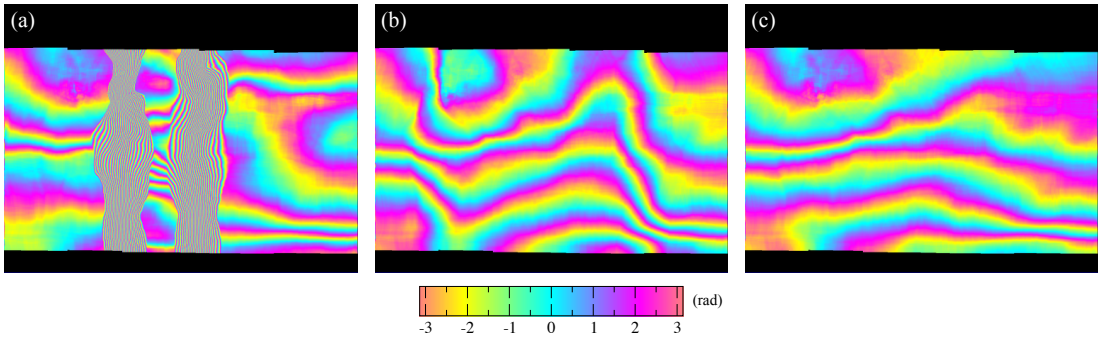

Fig. 9. A comparison of the different estimates of the differential ionospheric phase after filtering. (a) Moving center frequency to zero in the generation of subswath subband images using only subswath range starting time. (b) Moving center frequency to zero in the generation of subswath subband images using corrected subswath range starting time by subswath coregistration. (c) Relative phase error of subswath interferograms of (b) is further corrected. The relative phase errors between subswath interferograms of (a) are big, which leads to the two groups of dense fringes in (a) after filtering. Data acquired on Feb. 22, 2015 and May 3, 2015.

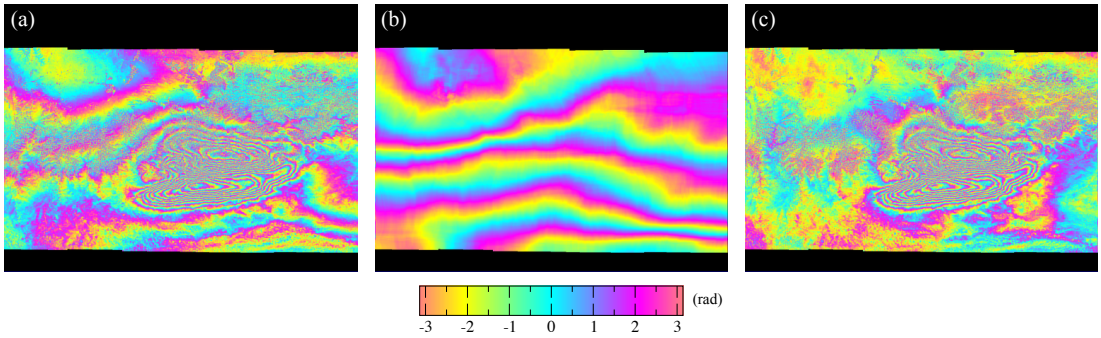

Fig. 10. Ionospheric correction result of ALOS-2 ScanSAR interferogram for April 25, 2015 *Mw*7.8 Nepal earthquake. (a) Original interferogram. (b) Estimated differential ionospheric phase. (c) Corrected interferogram. Data acquired on Feb. 22, 2015 and May 3, 2015.

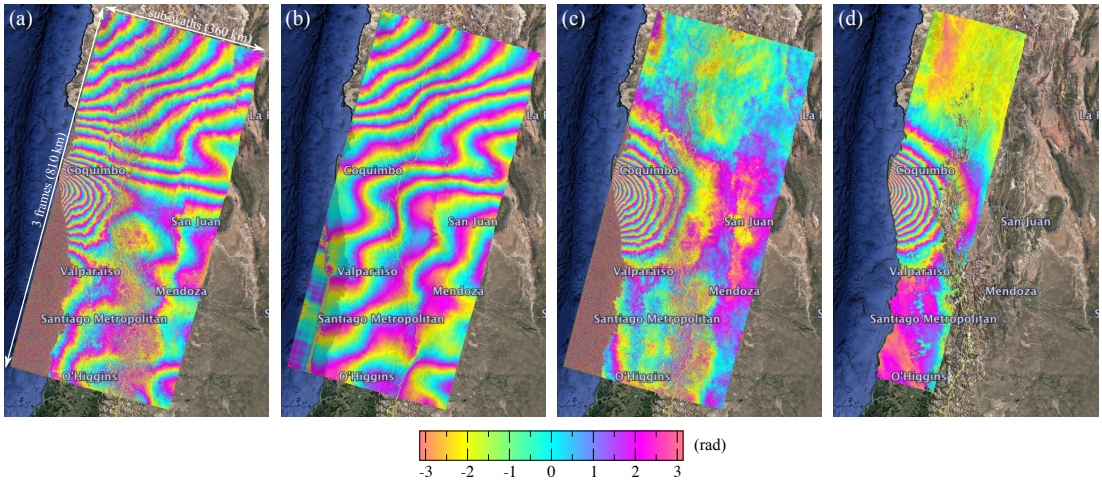

Fig. 11. Ionospheric correction result of ALOS-2 ScanSAR interferogram for September 16, 2015 *Mw*8.3 Chile earthquake. (a) Original interferogram. (b) Estimated differential ionospheric phase. (c) Corrected interferogram. (d) C-band Sentinel-1A TOPS interferogram after filtering, phase unwrapping and scaled according to the ratio of ALOS-2 and Sentinel-1A wavelengths. ALOS-2 ScanSAR data acquired on Jul. 30, 2015 and Sep. 24, 2015. Sentinel-1A TOPS data acquired on Aug. 24, 2015 and Sep. 17, 2015. Background image copyright Google Earth.

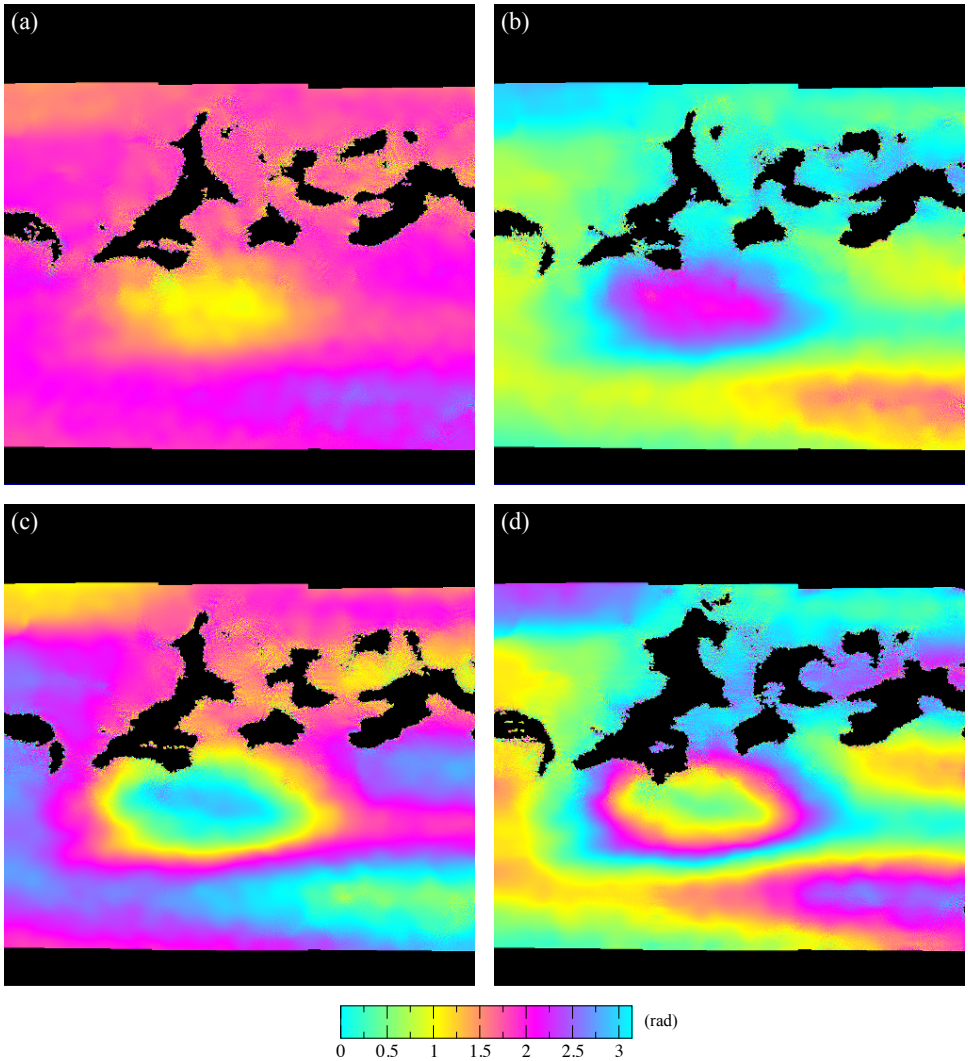

Fig. 12. MAI interferograms without phase correction. The time spans of the two look interferograms used to form MAI interferogram are (a) T_C. (b) $2T_C$. (c) $3T_C$. (d) $4T_C$.

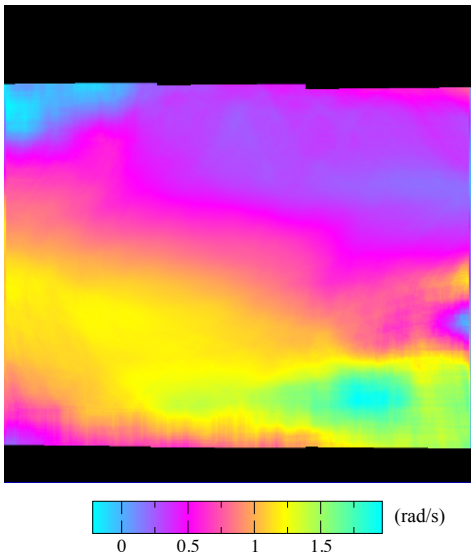

Fig. 13. The azimuth derivative of the differential ionospheric phase estimated using range split-spectrum method.

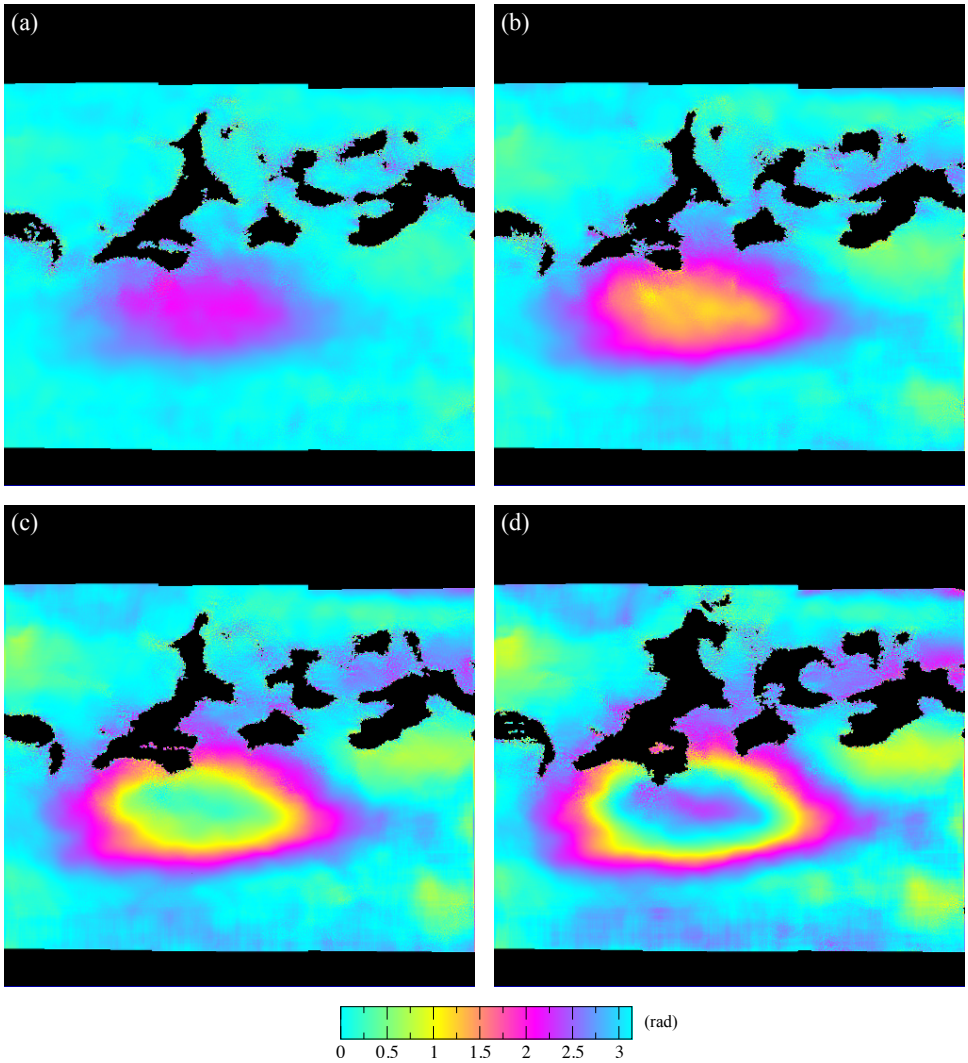

Fig. 14. MAI interferograms with phase correction. The time spans of the two look interferograms used to form MAI interferogram are (a) T_C. (b) $2T_C$. (c) $3T_C$. (d) $4T_C$.

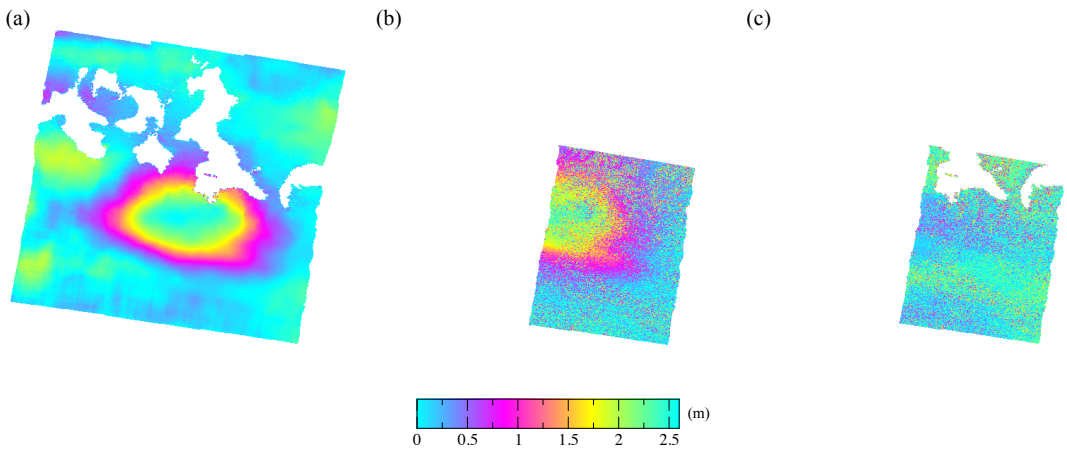

Fig. 15. Azimuth deformation of Nepal earthquake. (a) Result of ALOS-2 ScanSAR interferometry. (b) Result of incoherent cross correlation using a pair of high resolution Radarsat-2 images. (c) Difference.

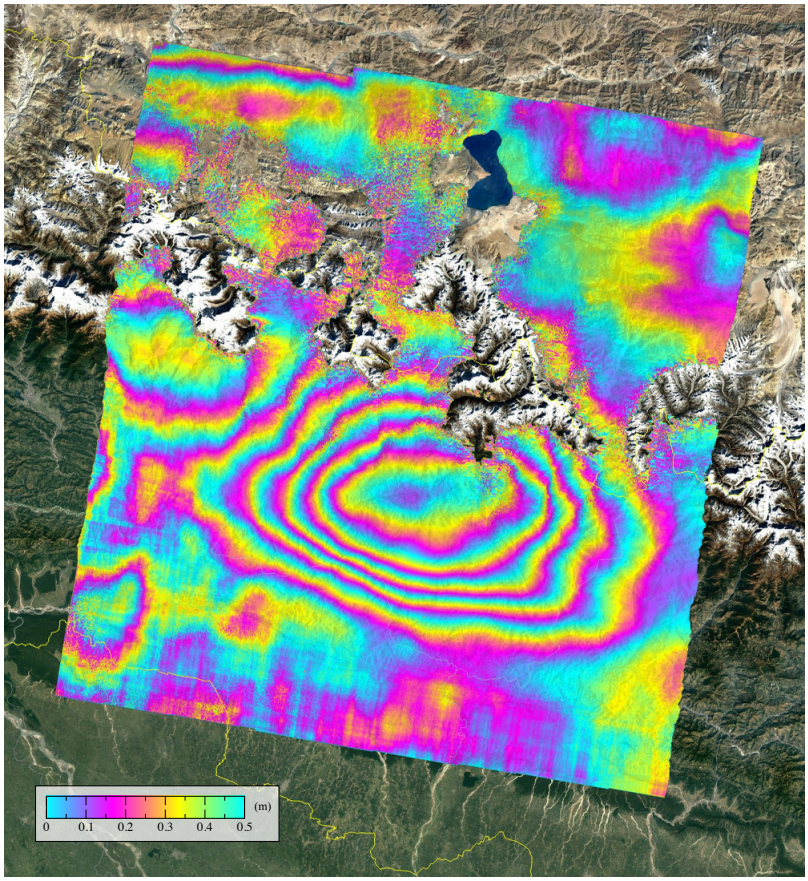

Fig. 16. Azimuth deformation of Nepal earthquake measured by ALOS-2 ScanSAR interferometry. Background image copyright Google Earth.

Table I Validation Results of the Exact Relationship between the MAI Phase ϕ_{MAI} and the Azimuth Derivative of Differential Ionospheric Phase $\partial\phi_{\mathrm{ion},d}/\partial\eta$ Given by Equation (15). MAI interferograms 1-4 are the ones shown in Fig. 12 (a)-(d). $-nT_C/2$ is the coefficient in equation (15), and a is the polynomial coefficient in equation (32).

MAI interferogram	$-nT_C/2$ [s]	a [s]
1	-0.392	-0.429
2	-0.784	-0.826
3	-1.176	-1.198
4	-1.568	-1.510